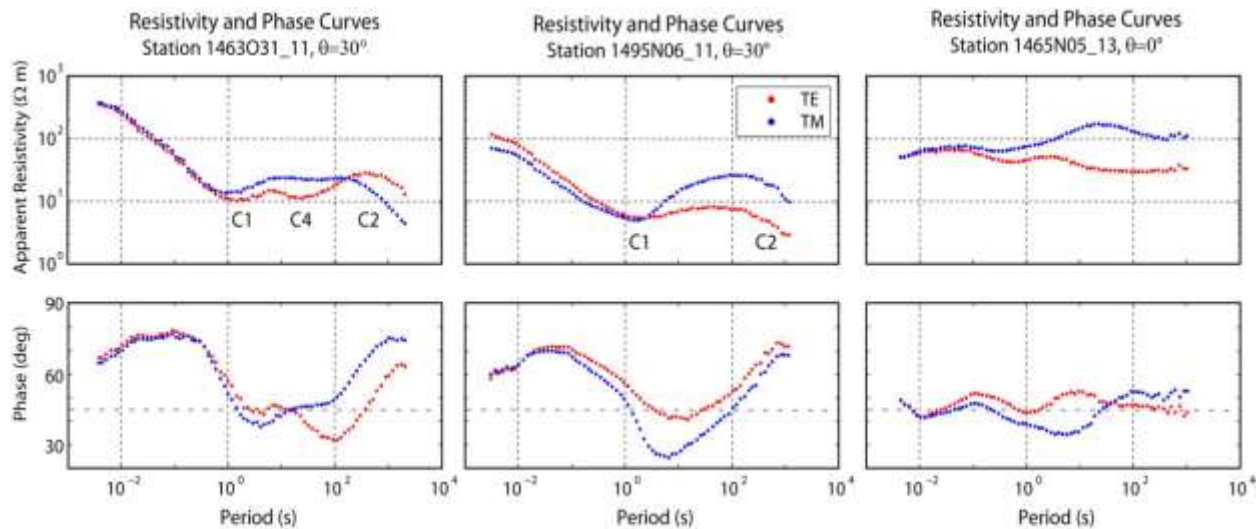


### 1. Magnetotelluric data

Owing to the remote location, and large distance from sources of electromagnetic noise, most stations were characterized by high quality MT data. Two typical MT soundings are shown in Figure S1. The shallow surface conductor (C1) causes the minimum in apparent resistivity at a period of  $\sim 2$  s, and the deeper conductor (C2) causes the decrease in apparent resistivity at periods greater than 300 s. An intermediate conductor representing a shallow magma body (C4) is seen at a period of  $\sim 20$  s at stations close to Volcan Uturuncu. In Figure S1, the data have been rotated to the strike direction determined by the dimensionality analysis in the following section. The transverse electric (TE) mode apparent resistivity is derived from electric currents flowing along strike and the transverse magnetic (TM) mode from currents flowing across strike.



**Figure S1.** Apparent resistivity and phase curves from station 1463O31 (on the west side of Volcan Uturuncu), 1495N06 (east of the volcano), and 1465N05 (in Argentina, near the end of the profile and on the edge of the APMB).

## **2. Dimensionality analysis**

**2.1 Tensor decomposition:** Dimensionality analysis determines if a 1-D, 2-D or 3-D resistivity model is needed to interpret the measured magnetotelluric (MT) data. In the case that the data can be considered 2-D, then tensor decomposition can estimate the geoelectric strike direction (Groom and Bailey, 1989).

### **2.1.1 Single site decompositions**

The first stage was to implement the tensor decomposition on a site-by-site basis. This allows a different strike to be computed at each station. The results are shown in both map view and as rose diagrams in Figure S2. It should be noted that strike directions determined with tensor decomposition have an inherent 90° ambiguity, and both possibilities are shown in the rose diagram in Figure S2 as red and blue wedges. In the maps, the length of the line represents the maximum phase split which is a measure of how non 1-D the MT impedance data can be considered. If the data is produced by a 1-D resistivity structure, then there is no variation in impedance with azimuth and the line will have zero length. The colour of the line shows the root-mean-square (r.m.s.) misfit between the measured MT data and the predictions of the tensor decomposition. This provides a measure of the validity of the tensor decomposition. Values with r.m.s. misfit less than 2 indicate that the assumptions are valid. The direction of the line in the map is the preferred strike direction chosen as one of the two orthogonal directions.

At short periods (1-10 s), there is no well defined strike direction since the EM signals are only sampling the near surface resistivity structure, which is approximately 1-D. At longer periods (10 -1000 s), the MT signals sample deeper in the Earth, and a well defined strike direction of N30°E can be observed for the whole dataset.

### **2.1.2 Multi site decompositions**

A second stage of the analysis is to determine if there is a strike direction that is applicable to all MT stations. This is required if a 2-D inversion is to be undertaken. This was implemented by fixing the strike direction at a given angle and determining the misfit for all stations and periods. Figure S3 shows the results of this for the Bolivia and Argentina profiles, as the fixed strike direction is varied. A clear minimum in the r.m.s. misfit can be seen in both curves.

A single r.m.s. value does not fully describe how well the data is fit. Thus Figure S4 shows the misfit as a function of station number and period for the preferred strike directions of N30°E in Bolivia and N0°E in Argentina. The generally low misfit values ( $< 2$ ) indicate that a 2-D approach is valid. Some areas with 3-D effects can be identified (e.g., near Volcan Quetena at distance of 40 km on the Bolivia section, and at isolated stations and at long periods on the Argentina profile).

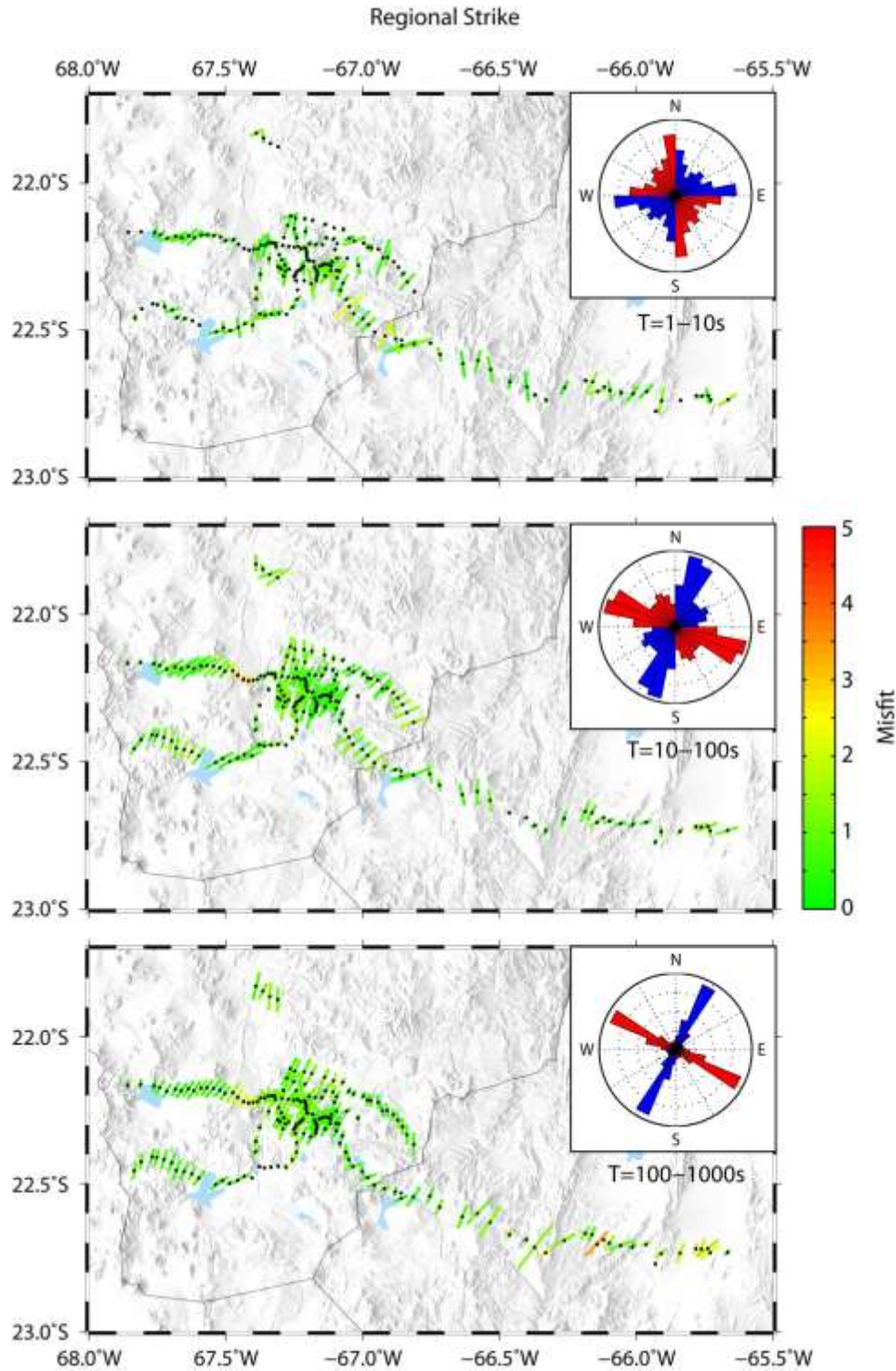


**Figure S2.** Results of tensor decomposition of the MT impedance data. There is no well defined strike direction for short periods. At longer periods ( $10 \text{ s} < T < 1000 \text{ s}$ ) a clear strike direction of N30°E is observed at stations in Bolivia. Figures S3 and S4 show that the strike is closer to N0°E in Argentina. However the rose diagram is dominated by the more numerous MT stations in Bolivia. Maps were created using the GMT package by Wessel & Smith (1991).

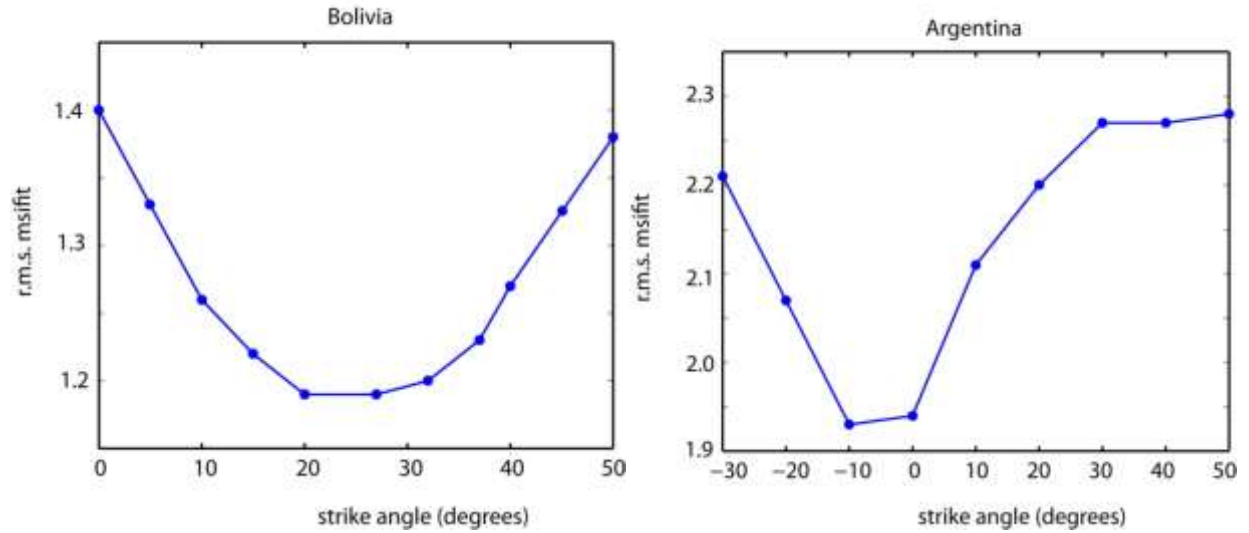


**Figure S3.** Fit of the measured MT impedance to the values predicted by tensor decomposition in the period band 1-1000 s. For each value of strike direction, a multi-site / multi-period decomposition was performed. The minima shows the preferred strike direction for all sites and periods included in the calculation. Error floor of 3% was used.

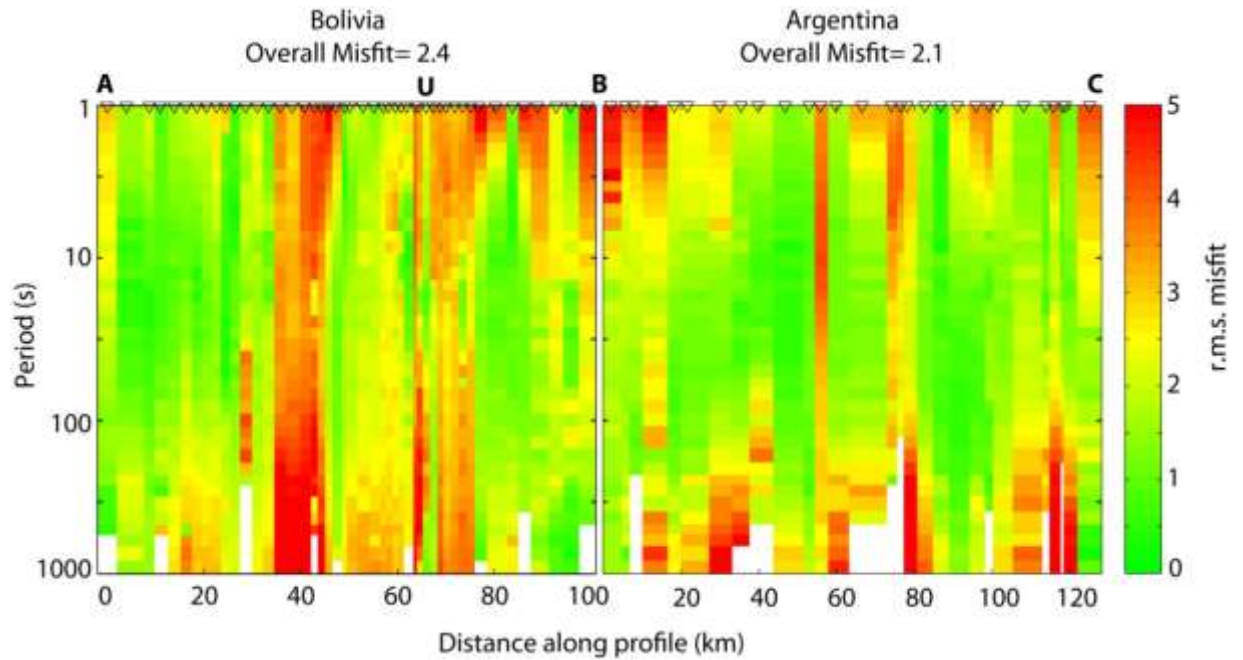


**Figure S4.** Pseudosections showing the fit of the tensor decomposition to the measured impedance data. This figure used a strike direction of N30°E for the stations in Bolivia and N0°E for stations in Argentina. It shows whether the assumptions made in the tensor decomposition are valid (i.e. if there exists a well defined strike direction for all stations and periods).

## 2.2 Induction vectors

Induction vectors are computed from the vertical magnetic fields generated by electric currents induced in the Earth. Their orientation can help eliminate the ambiguity of strike directions inherent in tensor decomposition. If the Earth has a 2-D resistivity structure, the real components of induction vectors will be orthogonal to the geoelectric strike direction. The real induction vectors are plotted in Figure S5 at a period of 294 seconds. Note the large amplitude vectors at the east end of the profile in Argentina. These define the eastern edge of the major conductor detected in the mid-crust by the 2-D inversion (C2 in Figure 2). Note that vertical magnetic fields were not measured at all MT stations.

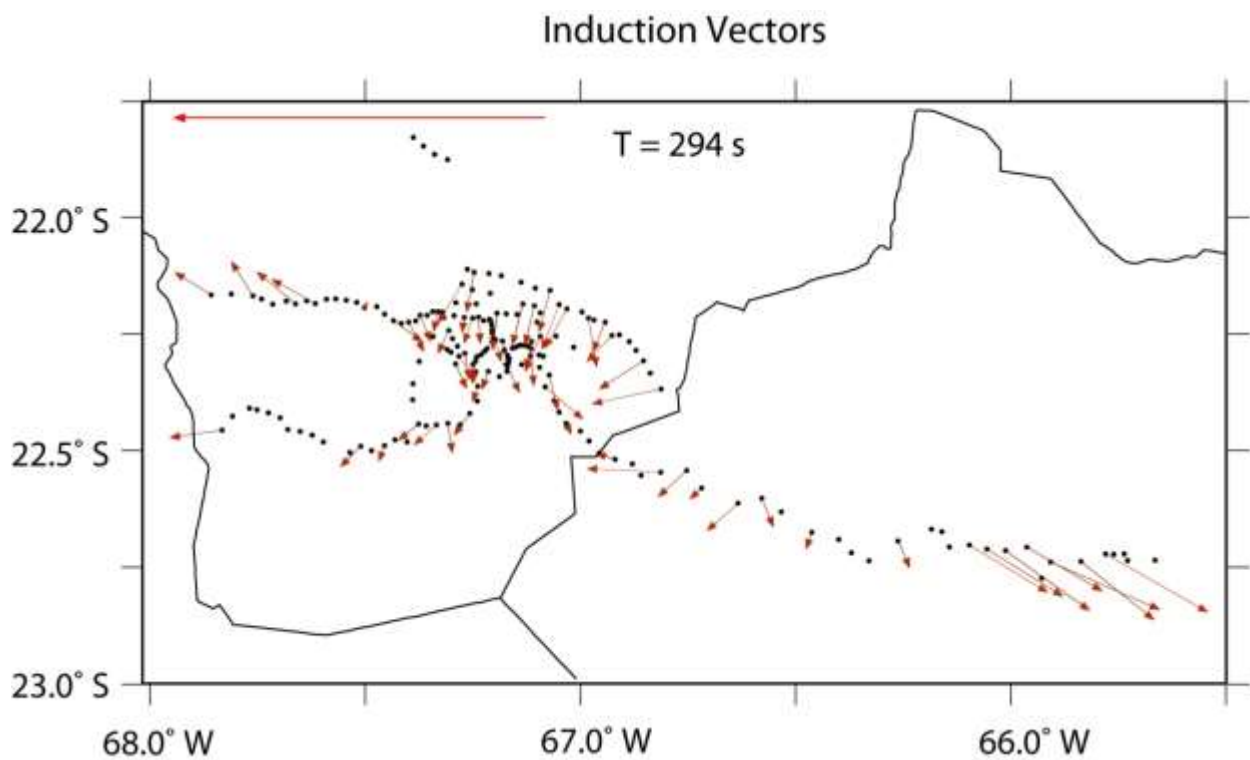


**Figure S5.** Real induction vectors at a period of 294 s. These are plotted using the Weise convention (i.e. pointing away from conductors). A scale arrow of unit magnitude is shown for reference.

## 2.3 Phase tensor

The phase tensor method (Caldwell et al., 2004; Bibby et al., 2005) is an alternative method to tensor decomposition for dimensionality analysis. It has the advantage that it is not necessary to assume that the subsurface resistivity structure is 2-D. The phase tensor is often visualized in map or pseudo-section view as an ellipse. The direction of greatest inductive response (equivalent to the 2-D geoelectric strike direction) aligns with one of the axes of the ellipse. Maps of the phase tensor ellipses at two representative periods are shown in Figure S6.

At a period of  $T = 3$  s the phase tensors plot as circles, showing that there is no preferred orientation at the depths sampled by these signals. The rose diagram shows the angle  $\alpha$ - $\beta$  which is equivalent to the strike direction. It can be seen that there is no preferred orientation. The colour fill indicates the skew angle is small, indicating a 1-D or 2-D resistivity structure.

At a period of  $T = 294$  s the phase tensors show a strong azimuthal dependence, with a preferred direction of N30°E. Skew values are higher in a couple of areas, notably close to Volcan Quetena (west of Volcan Uturuncu) and also in NW Argentina.

It is important to note that both tensor decomposition and phase tensor analysis give consistent estimates of the dimensionality and directionality of the subsurface resistivity structure. It appears that a 2-D MT inversion of these data is valid, although this will also be verified by using a 3-D MT inversion for selected parts of the study area.



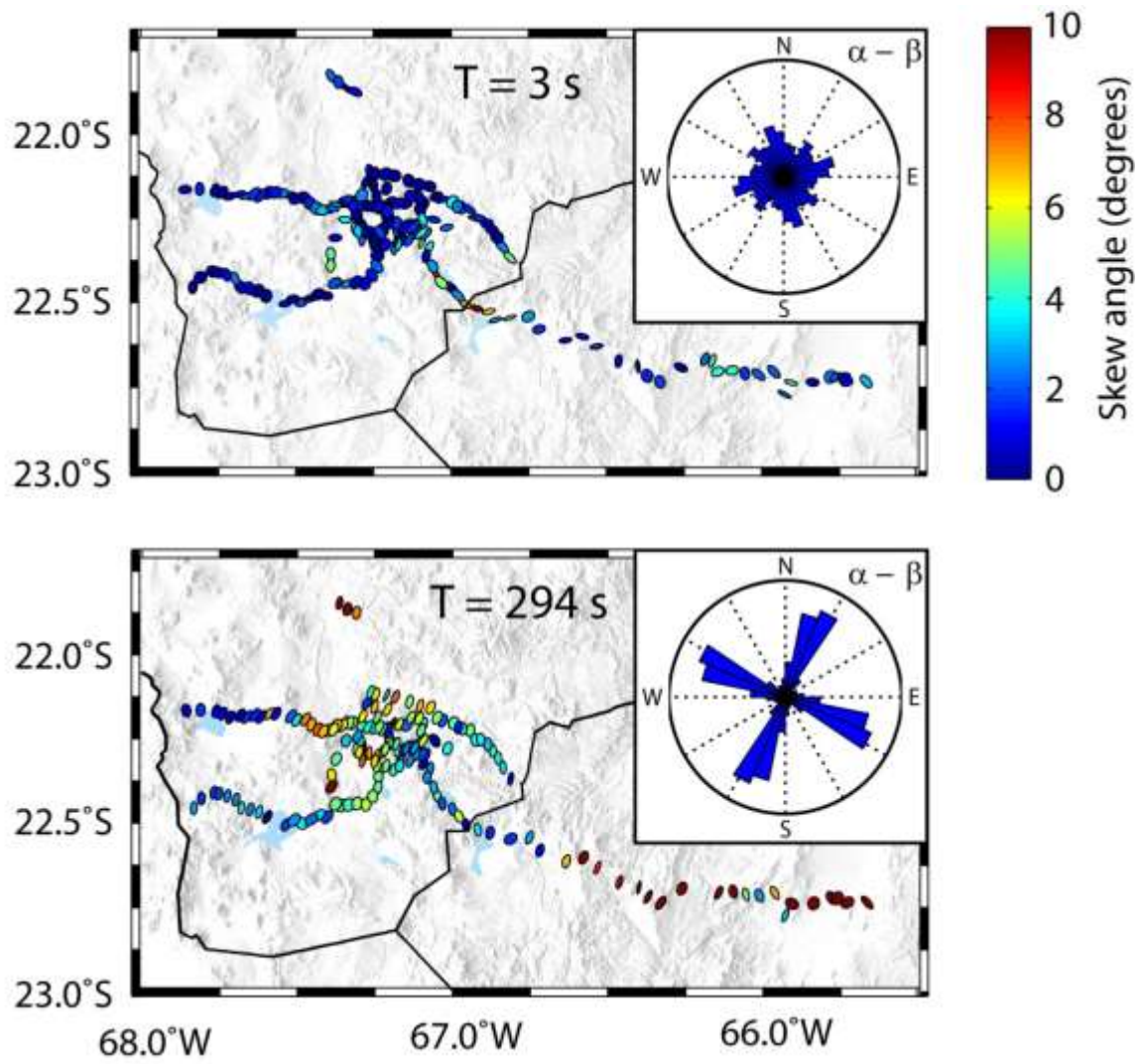


**Figure S6.** Phase tensor calculated at periods of 3 s and 294 s. At longer periods the phase tensors show a preferred direction of N30°E.

### **3. Inversion of magnetotelluric data**

#### **3.1 2-D Inversion**

The dimensionality analysis suggests that a 2-D inversion is valid for these MT data, with different strike directions determined for the two segments of the profile (i.e. in Bolivia and Argentina). Figure S7 shows pseudosections of the MT data for the profile AB in Bolivia, and Figure S8 shows the same quantities for the profile BC in Argentina. At long periods the data show low apparent resistivity and high phases. These can be associated with the deeper conductor (C2) in Figures 2 and 3.

For the 2-D inversions, the non-linear conjugate gradient algorithm of Rodi and Mackie (2001) was used to generate the resistivity models shown in Figure 2 of the paper. Error floors of 10% and 5% were used for the apparent resistivity and phase respectively. The inversion began with a 10  $\Omega\text{m}$  halfspace and included topography. After 200 iterations the r.m.s. misfit had been reduced from 13.4 to 1.49.

For the Argentina profile the parameters were similar. Slightly higher error floors of 20% and 10% were used, given the larger station spacing. After 200 iterations the r.m.s. misfit had been reduced from 10.4 to 1.48.

The 2-D inversion was repeated for a range of model regularization parameters, and after plotting an L-curve, a value of  $\tau = 10$  was chosen as representing the preferred compromise between fitting the measured MT data and producing a spatially smooth resistivity model, free of artefacts. The r.m.s. misfit at each station is plotted in Figure S9 and it can be seen that the data is fit uniformly.

MT data are often influenced by static shifts, that are due to near-surface resistivity structure that occurs at a small spatial length scale. These shifts are especially common in volcanic environments such as the study area, where there can be large changes in resistivity over a short horizontal distance (e.g., high resistivity lava flow and low resistivity zones of hydrothermal alteration). The inversion algorithm was allowed to estimate static shift coefficients and the values are plotted in Figure S10. These values represent the multiplicative shift applied to the resistivity curves at each of the corresponding stations. How much each feature will vary with depth depends on what period it is observed, the signal penetration depth (skin depth) scales as the square root of the static shift. The static shifts appear random across the profile and we observe no trends in them. They follow a Gaussian distribution and have a zero sum in log space. A range of methods was used to estimate static shifts and gave similar values.

Many combinations of inversion parameters were investigated, and the models in Figure 2 are representative. Factors investigated include variations in the strike direction, error floors and starting model.



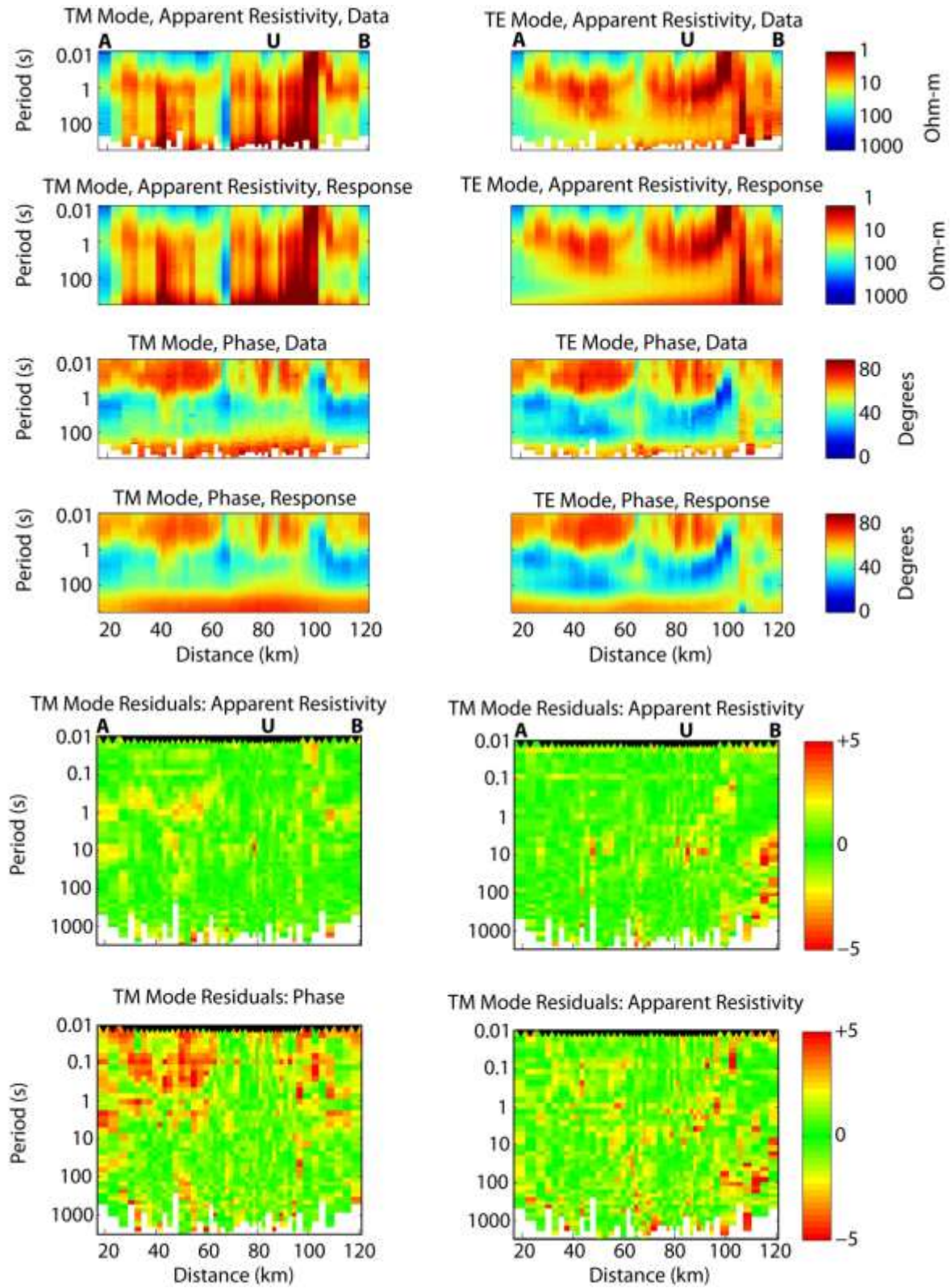


**Figure S7.** Pseudosections of measured MT data and the response of the inversion model for the MT profile AB in Bolivia. U = Volcan Uturuncu.

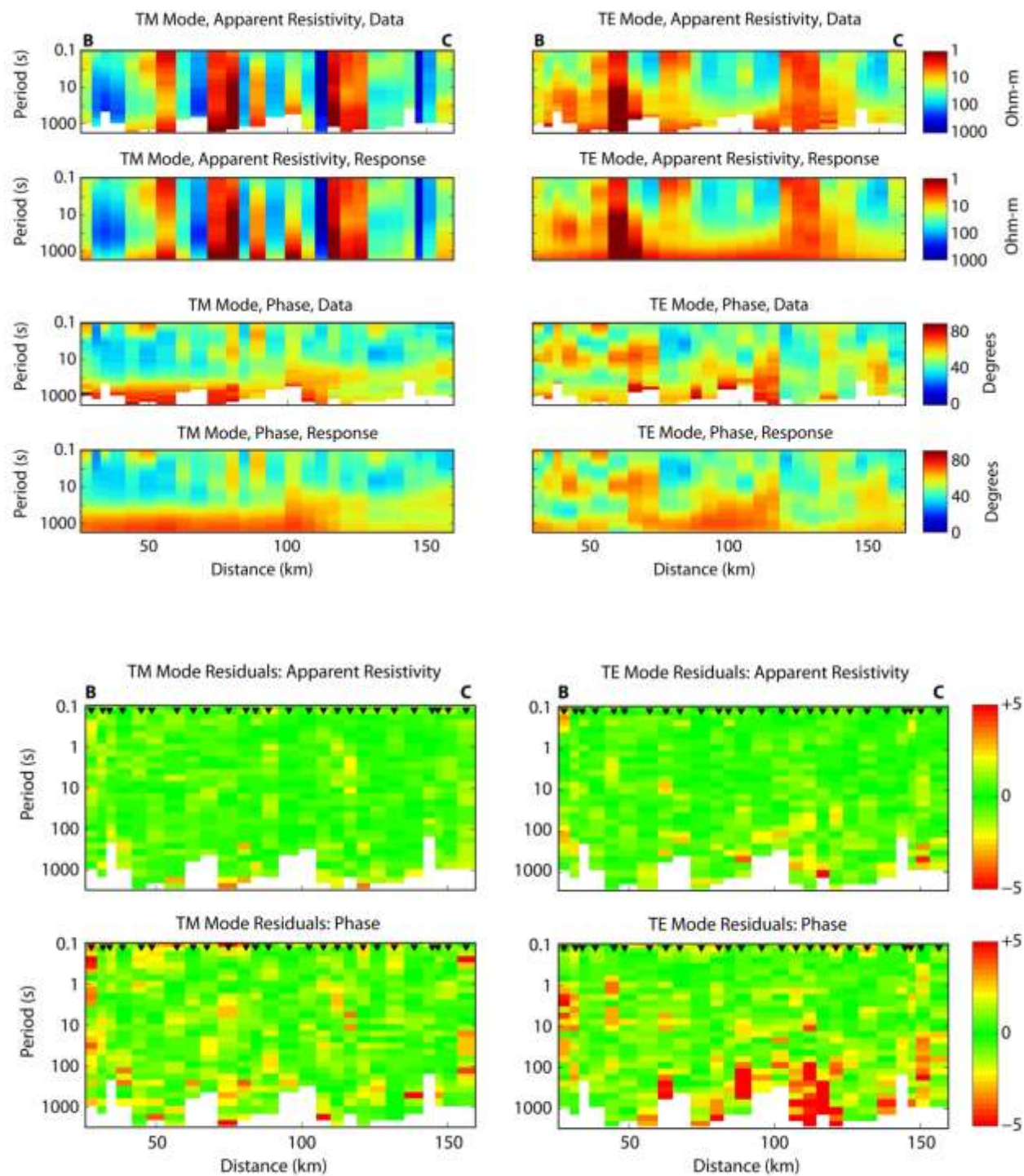


**Figure S8.** Pseudosections of measured MT data and the response of the inversion model for the MT profile BC in Argentina.

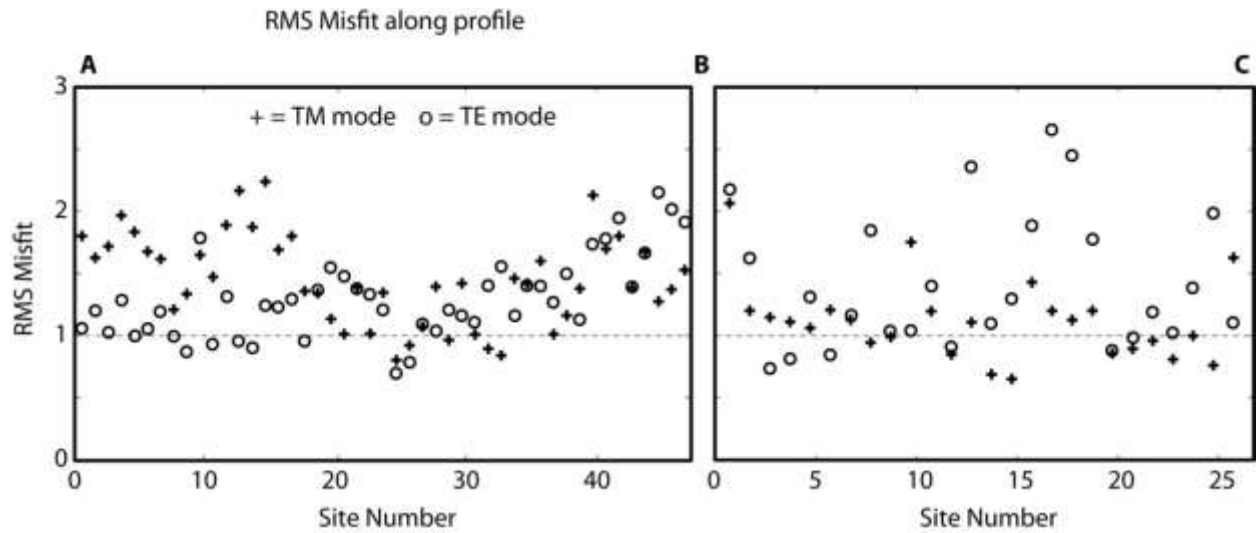


**Figure S9.** The r.m.s. misfit for the 2-D inversions. The ends of the profiles are denoted as points A, B, and C (shown in Figure 1). An r.m.s misfit of 1.0 implies the model fits within error (e.g., 10 %).

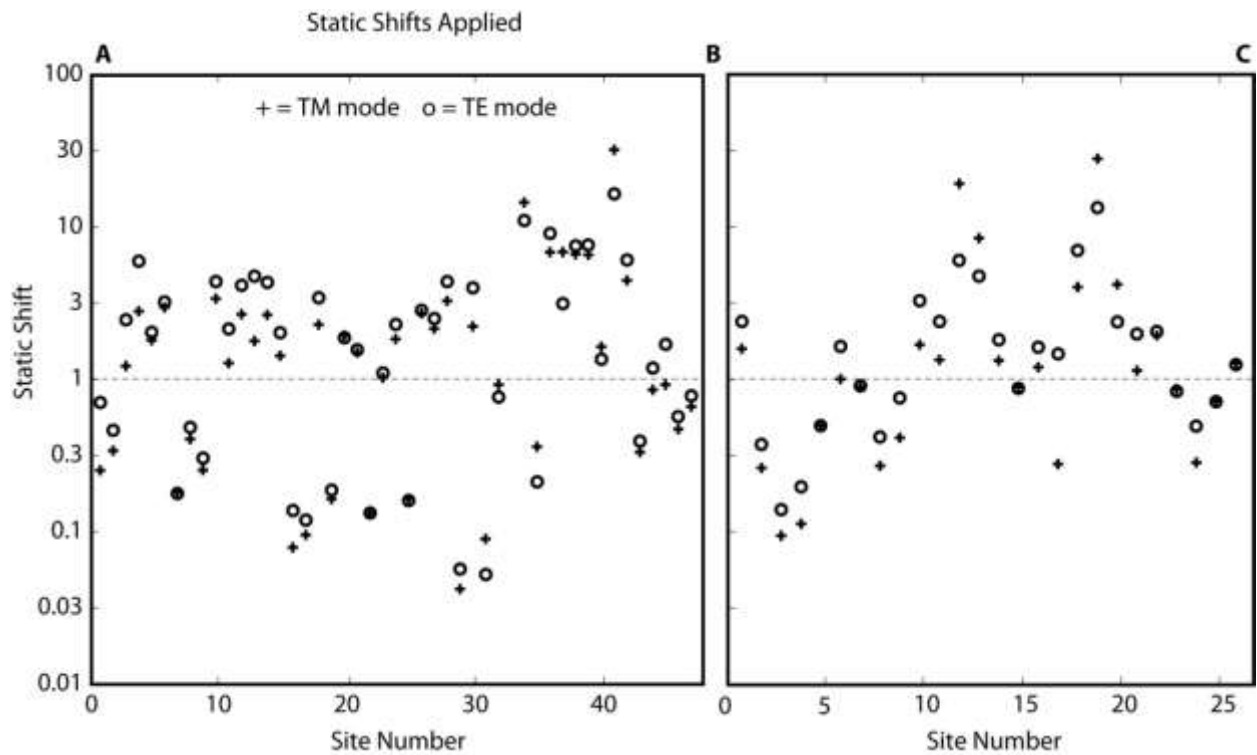


**Figure S10.** Static shift coefficients estimated by the 2-D inversions. These values represent the multiplicative shift applied to the resistivity curves at each of the corresponding stations (e.g., a value of 1 corresponds to no shift of the apparent resistivity).

### **3.2 3-D Inversion**

To test the reliability of 2-D inversion model, a subset of the MT data around Volcan Uturuncu were inverted using the 3-D inversion of Siripunvaraporn et al., (2005). The inversion model had 62 x 62 x 51 cells in the x, y, and z directions respectively. The inversion began from a 10  $\Omega\text{m}$  half space. Data at 73 stations with 18 periods in the band 0.01 - 1200 s were inverted. The inversion used the full impedance tensor with an error floor of 10%. After 7 iterations the r.m.s. misfit was reduced from 9.3 to 1.49. A second set of inversions was then begun, starting with the final model from the first stage. The fit of the apparent resistivity and phase data is illustrated in Figure S11.



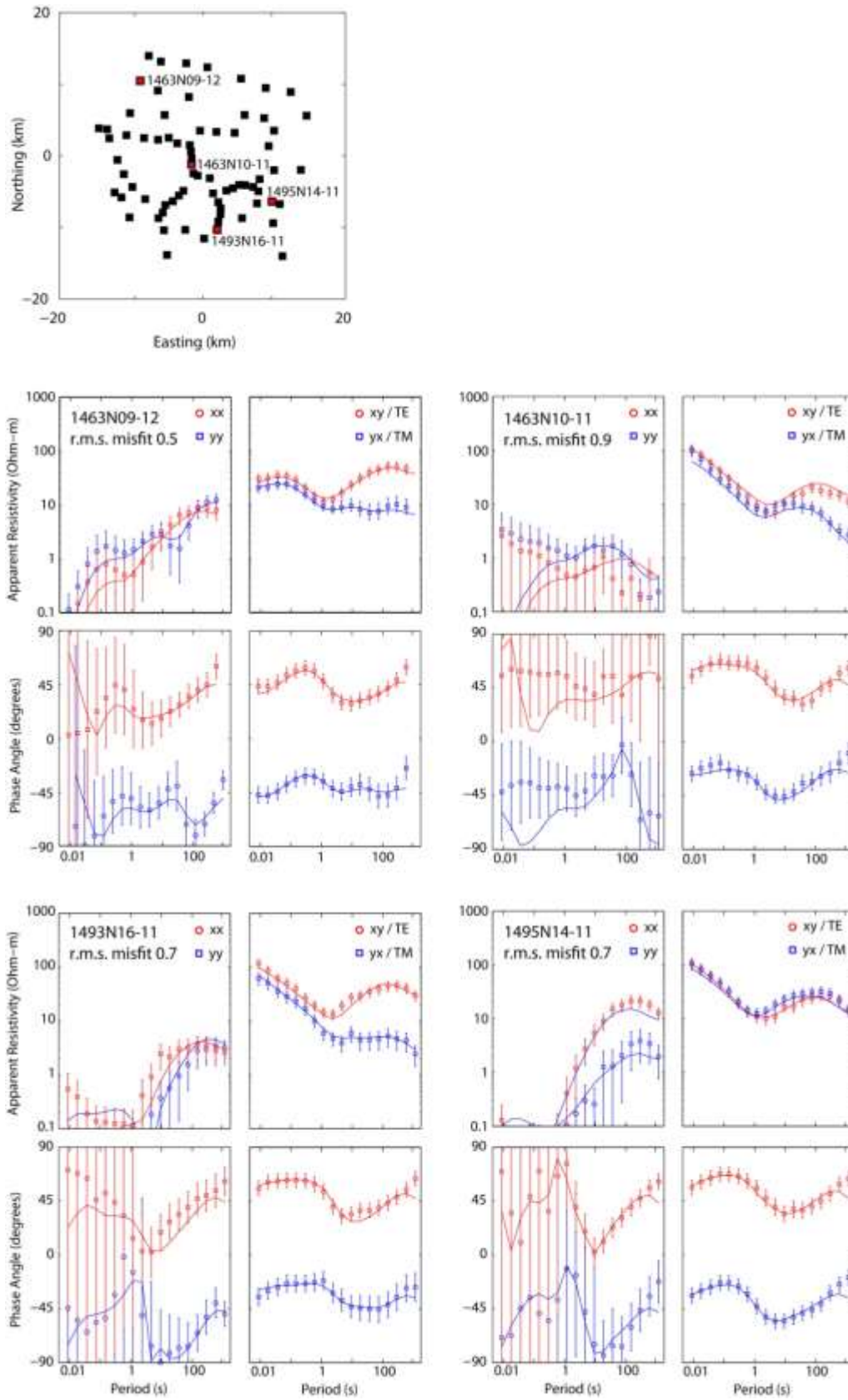


**Figure S11.** Data fit for the 3-D MT inversion at four representative stations. Red curves show XX and XY data computed from the north-south electric fields. Blue curves show the YX and YY data computed from the east-west electric fields.

### 3.3 Synthetic 3-D Inversion

Finally, the 3-D model was investigated using a set of synthetic inversions. The synthetic model incorporated

- Surface layer with a resistivity of 3  $\Omega\text{m}$ , 500m thick (to represent C1)
- A 100  $\Omega\text{m}$  resistive layer
- Conductive halfspace starting at 15 km below sea-level, 3  $\Omega\text{m}$  (to represent APMB/C2)
- Two narrow vertical conductors, 6 km thick with a resistivity of 3  $\Omega\text{m}$  (to represent intermediate conductors beneath Volcan Uturuncu, C4)

Synthetic data were computed in the period band 0.01-1500 s and 5% Gaussian noise was added. The same station geometry as in the actual study was used. Smoothing parameters of 0.2, 0.2, and 0.1 were chosen. The inversion began from a 10  $\Omega\text{m}$  starting model and after 4 iterations the r.m.s. misfit was reduced from 6.38 to 1.38. The original and final models are compared in Figure S12. Note that the depth of the conductive halfspace is recovered reliably, and the two intermediate conductors are distinguished. The geometry of the conductors is not fully recovered, owing to the irregular distribution of MT stations.



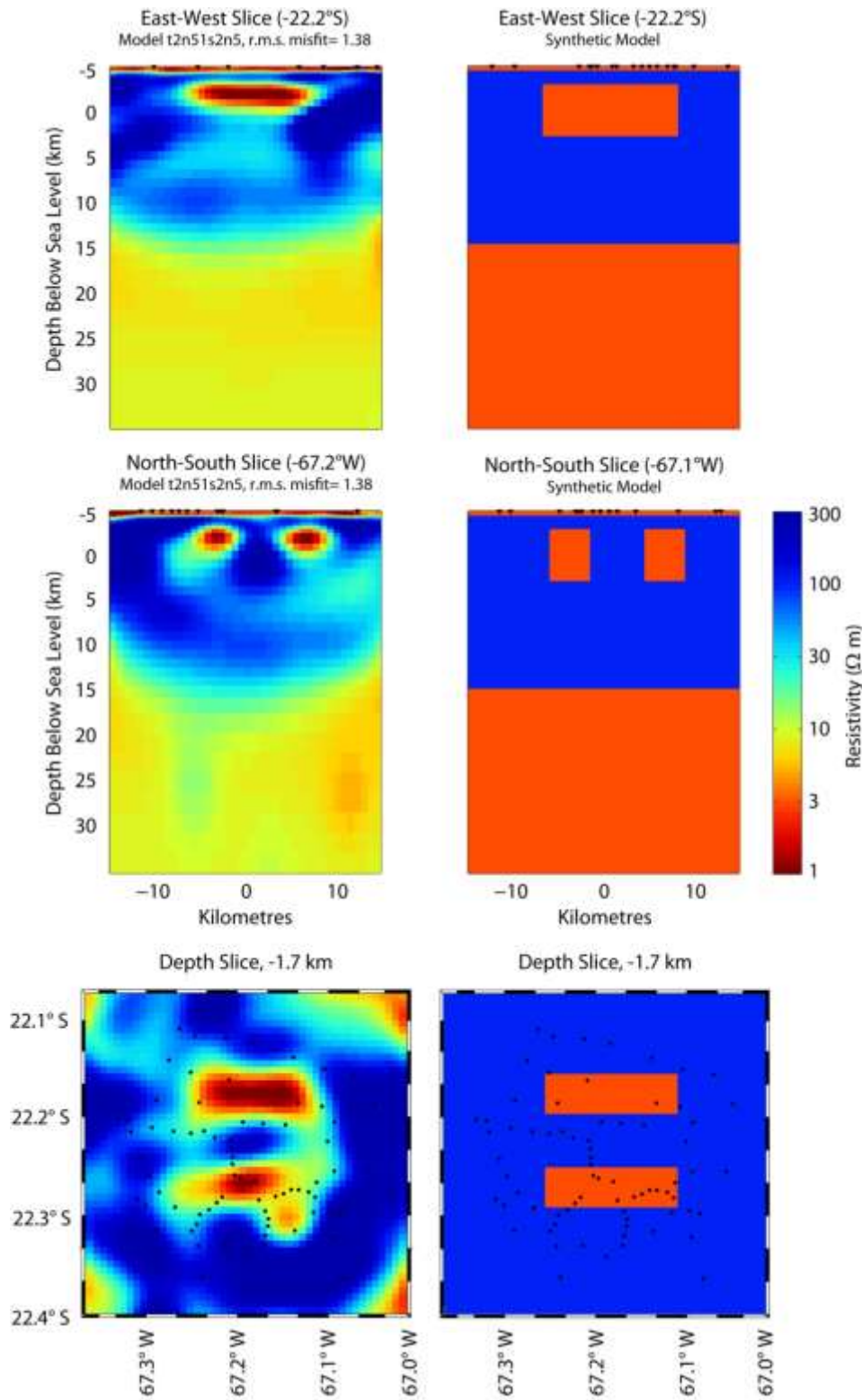


**Figure S12.** Results of a synthetic inversion used to investigate the sensitivity of the MT data. The panels on the right show the synthetic model, while those on the left show the recovered inversion model. The upper panels show East-West and North-South vertical sections. The lower panel shows a horizontal slice. The resistivity values and the geometry of the structure is well resolved.

#### **4. Calculation of melt fractions**

The resistivity values derived from MT exploration can be used to determine the composition of a magma body. However, this is a non-unique process since the bulk resistivity depends on several variables, including the melt composition, melt quantity and melt geometry. This approach was used for two magma bodies beneath Uturuncu, based on geochemical analysis of erupted lavas reported by Muir et al., (2014).

A dacite sample was taken to be derived from a magma body close to sea level with a silica content of 65% corresponding to C4 in Figure 2. Melt resistivity is dominated by the water and sodium contents (Pommier and Le Trong, 2011). The dacites had water content of 3-4%. The melt resistivity predicted for this composition and pressure is shown in Figure S13. Thermobarometry gives a temperature of 838°C which predicts a melt resistivity of ~5  $\Omega\text{m}$ . These are relatively high values for arc magmas and reflect the relatively low sodium content of the Uturuncu lavas. Since the magma body beneath Uturuncu has a resistivity of 1-3  $\Omega\text{m}$ , it is clear that the dacite melt cannot explain the observed resistivity. Another conducting phase is needed. This is illustrated in Figure S14 where the bulk resistivity of a rock containing 5  $\Omega\text{m}$  melt and 1000  $\Omega\text{m}$  rock grains is computed as a function of melt fraction.

This analysis was repeated for andesite lavas inferred to have been erupted from a deeper magma body beneath Volcan Uturuncu from their composition. These lavas had a silica content of 60%, a water content of 5-9% and  $\text{Na}_2\text{O}$  content of 2-3%. The combination of higher temperature (980 °C) and elevated sodium content gives the andesite magma a lower resistivity than the dacite magma (1 - 0.1  $\Omega\text{m}$ ), shown in Figure S13. When the lowest resistivity in this range (0.1  $\Omega\text{m}$ ) is combined with mineral grains of 1000  $\Omega\text{m}$ , it can be shown that a melt fraction in excess of 20% is needed to explain a bulk resistivity of 0.3  $\Omega\text{m}$  (Figure S14). These results are consistent with other researchers (e.g., Schilling, 2006).

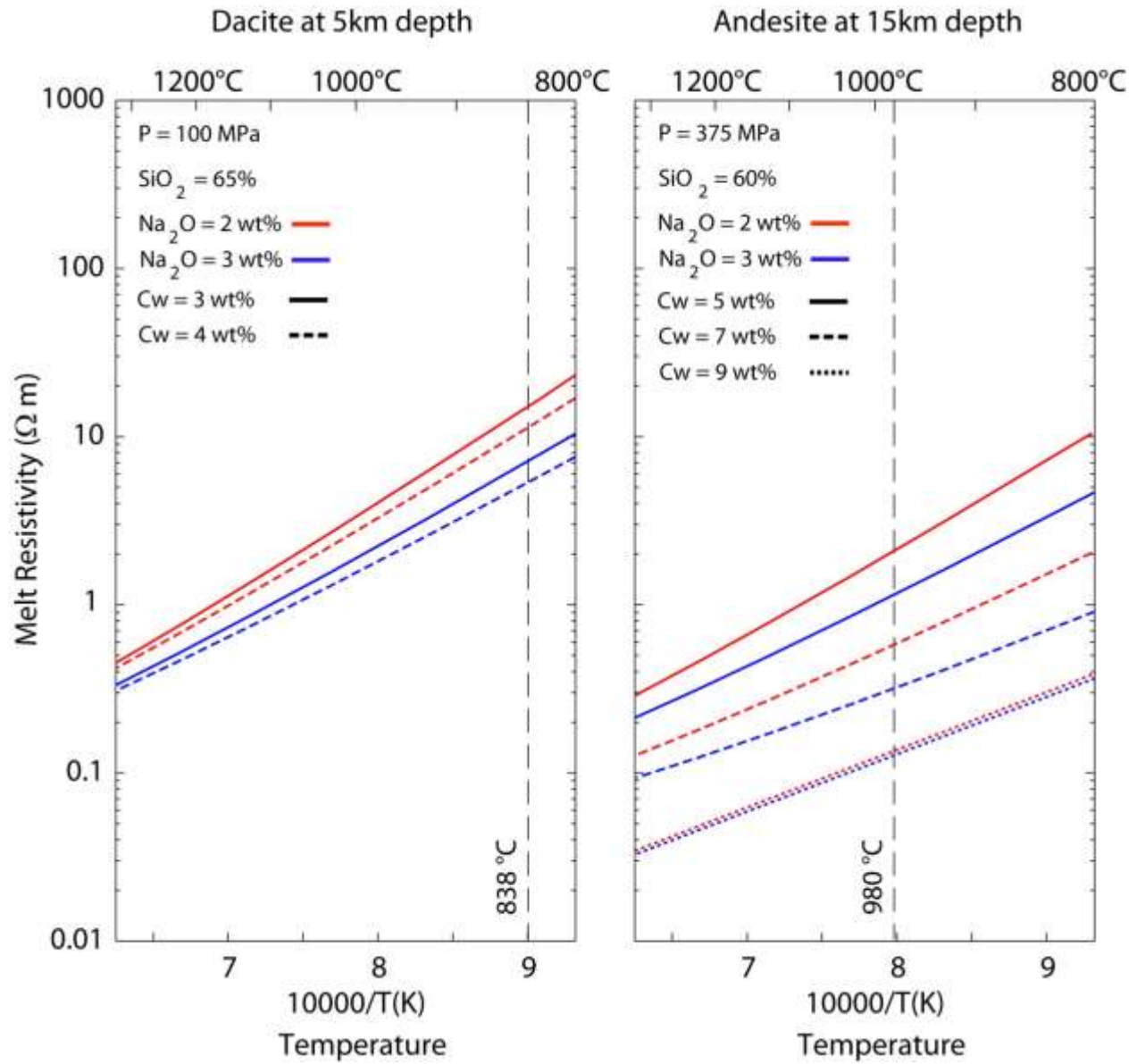


**Figure S13.** Variation of melt resistivity as a function of temperature for dacite and andesite melt with a range of water and sodium contents. The resistivity data were calculated using the SIGMELTS database of Pommier and Le Trong (2011). The lava composition was taken from Sparks et al., (2008). Depths are below surface, since this controls the pressure.

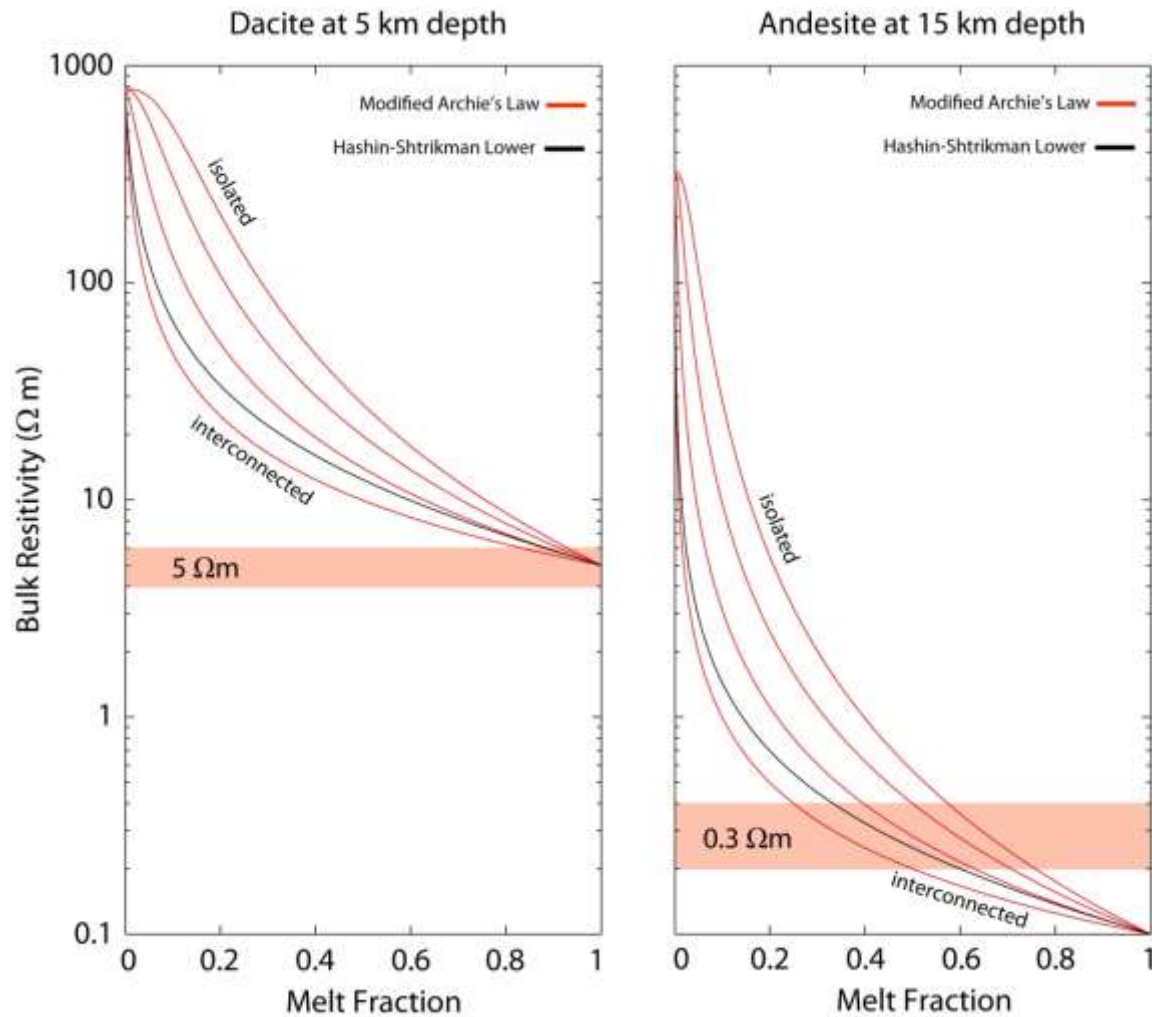


**Figure S14.** Bulk resistivity of a partially molten rock as a function of melt fraction for (a) dacite melt with resistivity of 5  $\Omega\text{m}$  and (b) andesitic melt with resistivity of 0.3  $\Omega\text{m}$ . The rock matrix is assumed to have a resistivity of 1000  $\Omega\text{m}$ . Red lines show the bulk resistivity, computed using the modified Archie's Law of Glover et al., (2000), for various degrees of melt interconnection (cementation factor  $m=1.0, 1.5, 2.0, 2.5$ ). The black line shows the Hashin-Shtrikman lower bound (upper bound is not shown), this is the preferred value since crustal melts are generally interconnected (ten Grotenhuis, 2005; Unsworth and Rondenay, 2013). Depths are below surface, since this controls the pressure ( $\sim 5$  km below surface = sea-level).

## References

Bibby, H. M., Caldwell, T. G., and Brown, C., (2005), Determinable and non-determinable parameters of galvanic distortion in magnetotellurics: *Geophysical Journal International*, 163, 915–930.

Glover, P., Hole, M.J., and Pous, J., 2000, A modified Archie's Law for two conducting phases: Earth and Planetary Science Letters, v. 180, p. 369-383.

Groom, R., and Bailey, R., 1989, Decomposition of Magnetotelluric Impedance Tensors in the Presence of Local Three-Dimensional Galvanic Distortion: Journal of geophysical Research, v. 94, p. 1913-1925.

ten Grotenhuis, S.M., Drury, M.R., Spiers, C.J., and Peach, C.J., 2005, Melt distribution in olivine rocks based on electrical conductivity measurements: Journal of Geophysical Research, v. 110.

Unsworth, M.J., and Rondenay, S., 2012, Mapping the distribution of fluids in the crust and lithospheric mantle utilizing geophysical methods, in Harlov, D.E., and Austrheim, H., eds., Metasomatism and the Chemical Transformation of Rock, Lecture Notes in Earth System Sciences: Berlin, Springer Verlag, v. 1, p. 535-598.

Wessel, P., and Smith, W., 1991, Free Software helps Map and Display Data: Eos, Transactions, American Geophysical Union, v. 72, p. 441-446.

### **5. Enlarged publication figures.**

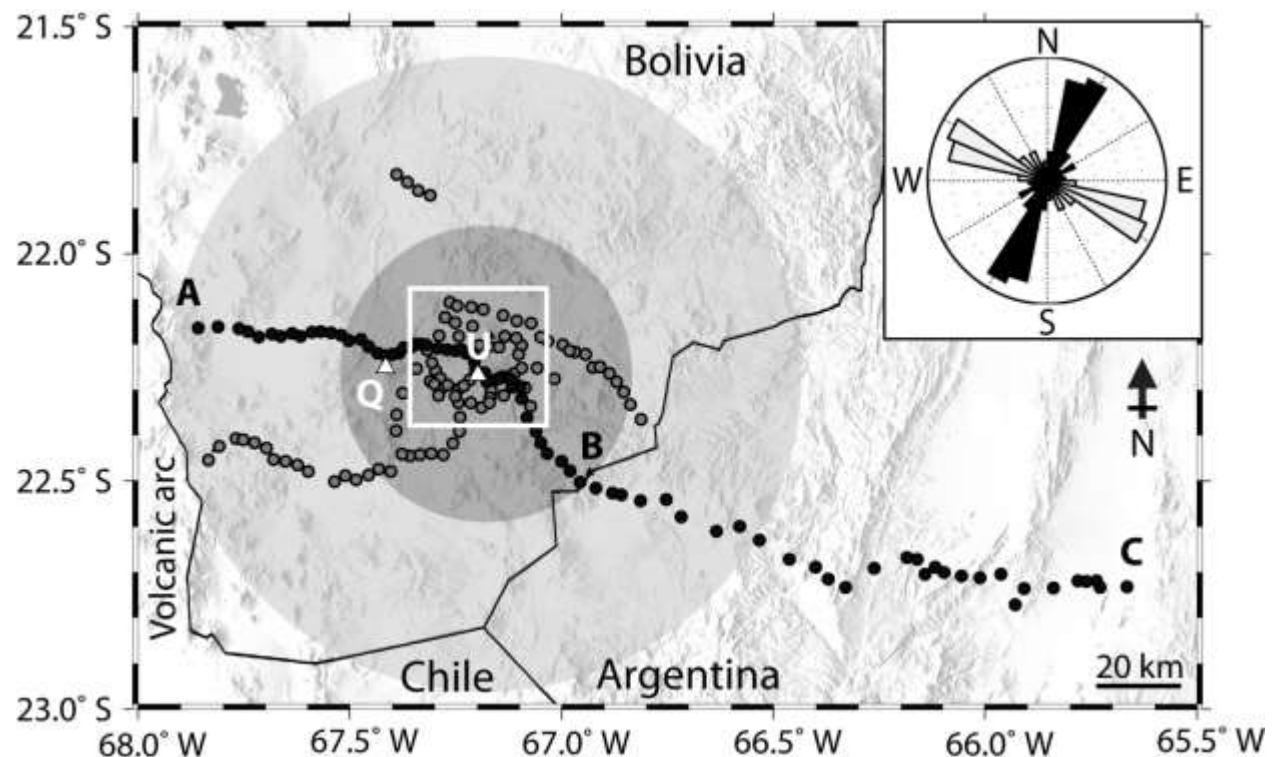


**Figure 1.**



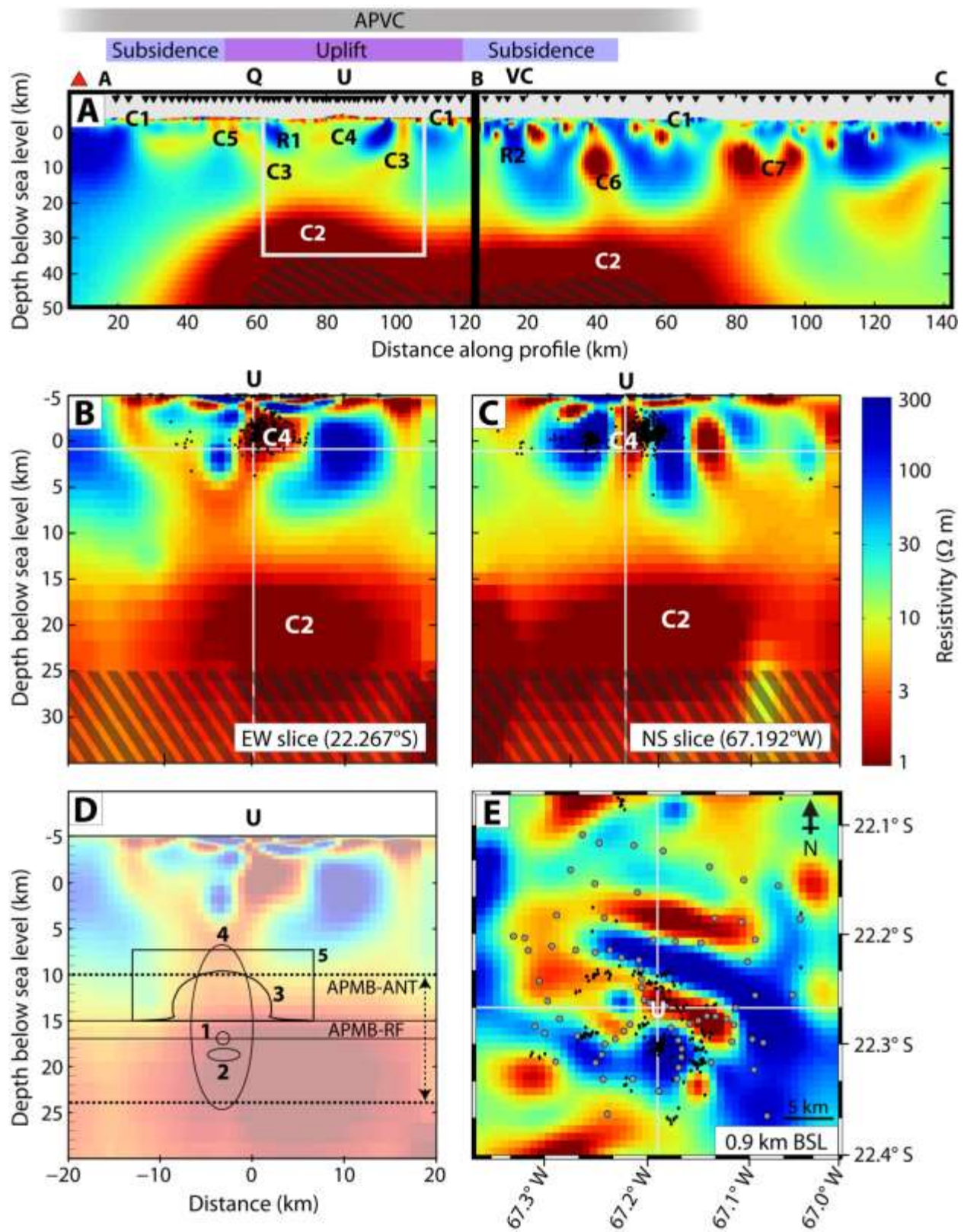


Figure 2.